

† These authors contributed equally to this work  
 \* Corresponding authors: sunnc@ucas.ac.cn, jfliu@nao.cas.cn

## A binary merger product as the direct progenitor of a Type II-P supernova

Zexi Niu<sup>†, 1, 2</sup> Ning-Chen Sun<sup>†\*, 1, 2, 3</sup> Emmanouil Zapartas<sup>†, 4, 5</sup> Dimitris Souroupanis, <sup>4</sup> Yingzhen Cui, <sup>2</sup> Justyn R. Maund, <sup>6</sup> Jeff J. Andrews, <sup>7, 8</sup> Max M. Briel, <sup>9, 10</sup> Morgan Fraser, <sup>11</sup> Seth Gossage, <sup>12, 13</sup>

Matthias U. Kruckow, <sup>9, 10</sup> Camille Liotine, <sup>12, 14</sup> Zhengwei Liu, <sup>15</sup> Philipp Podsiadlowski, <sup>16, 17</sup>

Philipp M. Srivastava, <sup>18, 12, 13</sup> Elizabeth Teng, <sup>14, 12, 13</sup> Xiaofeng Wang, <sup>19</sup> Yi Yang, <sup>19</sup> and Jifeng Liu<sup>\*2, 1, 3, 20</sup>

<sup>1</sup>School of Astronomy and Space Science, University of Chinese Academy of Sciences, Beijing 100049, China

<sup>2</sup>National Astronomical Observatories, Chinese Academy of Sciences, Beijing 100101, China

<sup>3</sup>Institute for Frontiers in Astronomy and Astrophysics,  
Beijing Normal University, Beijing 102206, China

<sup>4</sup>Institute of Astrophysics, Foundation for Research and Technology-Hellas, Heraklion GR-71110, Greece

<sup>5</sup>Physics Department, National and Kapodistrian University of Athens, Athens 15784, Greece

<sup>6</sup>Department of Physics, Royal Holloway, University of London, Egham TW20 0EX, United Kingdom

<sup>7</sup>Department of Physics, University of Florida, Gainesville FL 32611, USA

<sup>8</sup>Institute for Fundamental Theory, Gainesville FL 32611, USA

<sup>9</sup>Département d' Astronomie, Université de Genève, Versoix CH-1290, Switzerland

<sup>10</sup>Gravitational Wave Science Center (GWSC), Université de Genève, Geneva CH1211, Switzerland

<sup>11</sup>School of Physics, University College Dublin, Dublin 4 D04 P7W1, Ireland

<sup>12</sup>Center for Interdisciplinary Exploration and Research in Astrophysics (CIERA),

Northwestern University, Evanston IL 60201, USA

<sup>13</sup>NSF-Simons AI Institute for the Sky (SkAI), Chicago IL 60611, USA

<sup>14</sup>Department of Physics and Astronomy, Northwestern University, Evanston IL 60208, USA

<sup>15</sup>International Centre of Supernovae (ICESUN),

Yunnan Key Laboratory of Supernova Research, Yunnan Observatories,

Chinese Academy of Sciences (CAS), Kunming 650216, China

<sup>16</sup>London Centre for Stellar Astrophysics, London, United Kingdom

<sup>17</sup>University of Oxford, St Edmund Hall, Oxford OX1 4AR, United Kingdom

<sup>18</sup>Electrical and Computer Engineering, Northwestern University, Evanston IL 60208, USA

<sup>19</sup>Department of Physics, Tsinghua University, Beijing 100084, China

<sup>20</sup>New Cornerstone Science Laboratory, National Astronomical Observatories,

Chinese Academy of Sciences, Beijing 100012, China

Type II-P supernovae (SNe II-P) are the most common class of core-collapse SNe in the local Universe and play critical roles in many aspects of astrophysics. Since decades ago theorists have predicted that SNe II-P may originate not only from single stars but also from interacting binaries. While  $\sim 20$  SNe II-P progenitors have been directly detected on pre-explosion images, observational evidence still remains scarce for this speculated binary progenitor channel. In this work, we report the discovery of a red supergiant progenitor for the Type II-P SN 2018gj. While the progenitor resembles those of other SNe II-P in terms of effective temperature and luminosity, it is located in a very old environment and SN 2018gj has an abnormally short plateau in the light curve. With state-of-the-art binary evolution simulations, we find these characteristics can only be explained if the progenitor of SN 2018gj is the merger product of a close binary system, which developed a different interior structure and evolved over a longer timescale compared with single-star evolution. This work provides the first compelling evidence for the long-sought binary progenitor channel toward SNe II-P, and our methodology serves as an innovative and pragmatic tool to motivate further investigations into this previously hidden population of SNe II-P from binaries.

Keyword: Core-collapse supernovae, Type II supernovae, Massive stars evolution, Red supergiant stars

### I. INTRODUCTION

As the most common type ( $\gtrsim 50\%$  [1]) of core-collapse supernovae (SNe) in the local Universe, Type II-P refers to events whose spectra exhibit strong H features and whose light curves display a plateau phase for a few months powered by H recombination. They display a rich photometric and spectroscopic diversity, such as the plateau length, peak luminosity and expansion velocity

[2–4]. Understanding their origin is fundamental to unraveling the evolution of massive stars, the physics of their explosion, the lifecycle of the interstellar medium, the formation of compact objects, as well as the galactic chemical/mechanical feedback processes. The direct detection of  $\sim 20$  progenitors on pre-explosion images and analysis of their spectral energy distributions (SEDs) have confirmed that SNe II-P are exploding red supergiant (RSG) stars with massive H-rich envelopes [5–8].

It has now been well established that interacting binaries dominate the evolution of most massive stars [9] and the origin of most H-poor SNe (i.e. Types IIb, Ib, Ic and Ibn; [10–20]). For the H-rich SNe II-P, theoretical works have also predicted for decades that they may originate not only from single-star evolution but also from interacting binaries [10]. The elaborate binary pathways towards SNe II-P may include (1) the coalescence of two stars (merger), (2) the partial stripping of the initially more massive star (mass donor), or (3) the accretion onto an initially less massive companion (mass gainer). Recent studies quantify that as many as 30%–50% of all SNe II-P may have binary progenitors [21–25]. With a very wide parameter space (initial masses and orbital separation) and often very complicated interaction between the two member stars, binaries also serve as a promising candidate to explain what drives the observational diversity of SNe II-P.

Compelling observational evidence, however, still remains elusive for this speculated binary progenitor channel toward SNe II-P. In both the single and binary channels, a SN II-P progenitor before core collapse will similarly appear as a RSG based on effective temperature and luminosity [21, 22, 24, 26]. The SN spectra will neither exhibit any obvious signatures of binary interaction since most differences in the progenitor’s chemical abundance profiles caused by material mixing during mass transfer will be erased in the subsequent stellar evolution. Survived binary companions are not expected to be found for the merger and mass gainer progenitors [22, 27] while the mass donor progenitors, which may possibly have survived binary companions, account for only <5% of SNe II-P as they require fine-tuned orbital separations to retain sufficiently massive H-rich envelopes [21]. Therefore, the binary progenitor channel for SNe II-P still remains an outstanding challenge in astrophysics.

A key prediction from theoretical population synthesis is that many merger and mass gainer progenitors have longer evolutionary timescales compared to single-star progenitors of equivalent RSG luminosity and He-core mass [28–30]. Thus, an innovative methodology to uncover the potential binary nature of SN II-P progenitors is to identify them in older stellar environments than those consistent with single-star evolution [30, 31]. In addition, binary progenitors, depending on the mass-transfer history, may have very different core-to-envelope mass ratios compared to single-star progenitors [24, 32], and this can lead to unusual plateau lengths in the resultant SN light curves compared with those from single-star progenitors [21].

In this work, we report the identification of a RSG progenitor for the Type II-P SN 2018gj. We provide compelling observational evidence for its origin from an interacting binary system and reveal its pre-SN evolution with state-of-the-art binary evolution simulations. This study confirms that interacting binaries are indeed a viable progenitor channel toward SNe II-P and establishes a successful methodology that can motivate future investi-

gations to uncover a previously hidden population of SNe II-P from binaries.

## II. PROGENITOR DETECTION

SN 2018gj is a Type II-P event located in the outskirt of the nearby galaxy NGC 6217 (Fig. 1a) with a heliocentric redshift of  $z = 0.004540$ . The site of SN 2018gj was observed by the HST several times before and after its explosion with the Wide Field Channel (WFC) of the Advanced Camera for Surveys (ACS) and the Ultraviolet-Visible channel (UVIS) of the Wide Field Camera 3 (WFC3). A full list of these observations is provided in Table 1. We retrieved the images that have been flat-fielded and corrected for charge transfer efficiency (i.e. `*_f1c.fits`) from the Barbara A. Mikulski Archive for Space Telescopes (MAST; <https://mast.stsci.edu>). For the post-explosion images, we manually combined the exposures with the ASTRODRIZZLE package for better cosmic-ray removal by setting `driz_cr_grow = 3`. The pre-explosion observations adopted an unusually large dithering distance of 2048 pixels and an exposure at only one of the dithering positions covered SN 2018gj; for these images, we removed the cosmic rays with Laplacian edge detection [34, 35].

We used the DOLPHOT package [36] for point-spread-function (PSF) photometry with parameters recommended in the user manual. On the post-explosion images taken in 2019, 2021 and 2023 (Fig. 1g–l), a continuously fading source is detected near the reported coordinates of SN 2018gj,  $(\alpha, \delta)_{J2000} = (16:32:02.300, +78:12:40.9)$ . We identified this fading source as the late-time radiation of SN 2018gj. We then performed differential astrometry between the pre- and post-explosion images taken in 2019 with 10 common stars, which allowed us to determine the SN position on the pre-explosion images with an accuracy of 0.83 pixels. A point source was significantly detected on the pre-explosion F625W and F814W images (Fig. 1e and f) at the derived SN position with an offset of only 0.16 pixels, much smaller than the astrometric uncertainty. On the pre-explosion F435W and F658N images (Fig. 1c and d), no source is detected at the SN position at a  $3\sigma$  level. We determined the detection limit by inserting artificial stars with different magnitudes at the SN position; the detection limit corresponds to the magnitude where the  $3\sigma$  source detection probability falls to 50%. The last column of Table 1 lists the photometry of this source and SN 2018gj at late times.

We suggest that this pre-explosion point source corresponds to the progenitor of SN 2018gj. The SN is located in a very sparse area, so chance alignment with an unrelated celestial object is very unlikely, and we estimated a chance-alignment probability of only 0.004% based on the surface density of sources in this area. The detected progenitor is neither due to an unrejected cosmic ray, since a randomly positioned cosmic ray will co-

incide with SN 2018gj within the positional error circle with a very low probability of 0.012%. Furthermore, the SHARPESS parameter returned by DOLPHOT is  $-0.007$ , very close to zero; this suggests that the morphology of the detected progenitor matches the PSF very well, while cosmic rays are usually much sharper than the PSF. The F814W brightness of SN 2018gj in 2021 and 2023 becomes much fainter than the progenitor, suggesting that it has disappeared after the SN explosion. We notice that although the F814W brightness in 2021 and 2023 is higher than a simple extrapolation of the light curve tail, this could be attributed to a light echo or CSM interaction, which are commonly observed in many SNe (e.g., Refs. [16, 37]).

SN 2018gj was also observed with the Spitzer/IRAC at 3.6 and  $4.5\text{ }\mu\text{m}$  in 2009 and 2019. We retrieved the post-basic calibrated data (PBCD) images from the Spitzer Heritage Archive<sup>1</sup>. The SN is clearly visible in both bands in 2019, but no pre-explosion counterpart can be detected at the SN position in the 2009 images. Differential astrometry with 16 common stars is applied, achieving a precision of  $0.06/0.18$  pixels for  $3.6/4.5\text{-}\mu\text{m}$  band. Based on the local background flux densities around the SN position, we estimated  $3\text{-}\sigma$  detection limits for the progenitor of  $[3.6] > 16.5$  mag and  $[4.5] > 15.9$  mag. Zeropoints and conversion factors between flux density and Vega magnitudes were adopted from the IRAC Instrument Handbook<sup>2</sup>. The model SEDs adopted in our analysis (see below) predict pre-explosion magnitudes of about 21 mag at  $[3.6]/[4.5]$  for the progenitor system, much fainter than the detection limits. While these limits are not sufficiently deep to provide meaningful constraints on progenitor SED models, we include them here for completeness.

Fig. 2a displays the SED of the SN progenitor. We fit the observed SED of SN 2018gj's progenitor with the MARCS model atmospheres with a solar metallicity, assuming a microturbulent velocity of  $5\text{ km s}^{-1}$  and surface gravity  $\log(g) = 0\text{ dex}$  (broad-band photometry is not sensitive to the values of these two parameters). Values of distance, metallicity and line-of-sight reddening are discussed in the Supplementary Materials. The effective temperature and bolometric luminosity were left as free parameters to be fitted. We calculated synthetic magnitudes by convolving the model atmospheres with the HST filters' response curves, which were then compared with the observed magnitudes or detection limits. We derived the posterior probability distributions with a Markov-Chain Monte-Carlo method and found an effective temperature of  $\log(T_{\text{eff}}/\text{K}) = 3.54 \pm 0.01$  and a luminosity of  $\log(L/L_{\odot}) = 5.0 \pm 0.1$ , corresponding to a radius of  $875 \pm 140 R_{\odot}$ . The uncertainties were propagated from

those in the photometry, distance and reddening. Fig. 2b plots the position of the progenitor on the Hertzsprung-Russell diagram (HRD); other confirmed SN II-P progenitors are overlaid for comparison.

For RSGs, the final He-core mass and final luminosity follow a tight relation [26]:

$$\log(M_{\text{He}}/M_{\odot}) = 0.659 \times \log(L/L_{\odot}) - 2.630; \quad (1)$$

therefore, the progenitor of SN 2018gj had a final He-core mass of  $M_{\text{He}} = 4.6 \pm 0.7 M_{\odot}$ . Assuming single-star evolution, this corresponds to an initial mass of  $M_{\text{ini}} = 13\text{--}16 M_{\odot}$  and an age of  $\log(t/\text{yr}) = 7.1\text{--}7.3$  based on the BPASS [39] and BINARY\_C [40] single-star evolutionary tracks. The results from POSYDON single star models [41, 42] yield  $M_{\text{ini}} = 12\text{--}15 M_{\odot}$  and  $\log(t/\text{yr}) = 7.2\text{--}7.4$ . These three models are mainly used in the following analysis. These values are also consistent with results based on other stellar evolutionary models (i.e. KEPLER, HOSHI [43]).

Another probe of the progenitor state, especially its core mass, comes from the  $[\text{O}i] \lambda\lambda 6300, 6363$  doublet flux at nebular phase, which for SN 2018gj is in good agreement with the model spectrum of an initial progenitor mass of  $15 M_{\odot}$  [33]. This agreement has also been verified through a separate analysis ([43], private communication). This independent measurement is consistent with the single-star equivalent initial mass from our progenitor detection.

Some SNe II-P progenitors are subject to circumstellar extinction and brightness variability due to pulsations, which may influence the luminosity/mass estimate based on direct progenitor detections. The color of SN 2018gj progenitor, when corrected for (Galactic and host) interstellar extinction, agrees well with that of a RSG and does not show any obvious color excess arising from circumstellar extinction. Besides, no significant dust emission can be detected at the SN position on the  $3.6\text{-}$  and  $4.5\text{-}\mu\text{m}$  pre-explosion Spitzer/IRAC images. Therefore, it seems unlikely that the derived progenitor Pulsational variability of the progenitor's luminosity [44–46] has been inferred in various event, such as SN 2017eaw [47], SN 2023ixf [7, 48, 49], SN 2024ggi [8], and SN 2025pht [50], which may influence the inferred pre-SN core mass estimate. In an extreme case that SN 2018gj is analogous to the case of SN 2023ixf with which it has similar progenitor luminosity, its value may vary by up to 0.25 dex [49], with pulsations being the dominant source of uncertainty. This would imply a lower limit of the final He-core mass of  $M_{\text{He}} \approx 3.2 M_{\odot}$ , which we further discuss in the context of our results in Section III C.

### III. SINGLE OR BINARY EVOLUTION?

While the directly detected progenitor of SN 2018gj resembles those of other SNe II-P in terms of effective temperature and luminosity, SN 2018gj exhibits two distinc-

<sup>1</sup> <https://sha.ipac.caltech.edu>

<sup>2</sup> <https://irsa.ipac.caltech.edu/data/SPITZER/docs/irac/iracinstrumenthandbook>

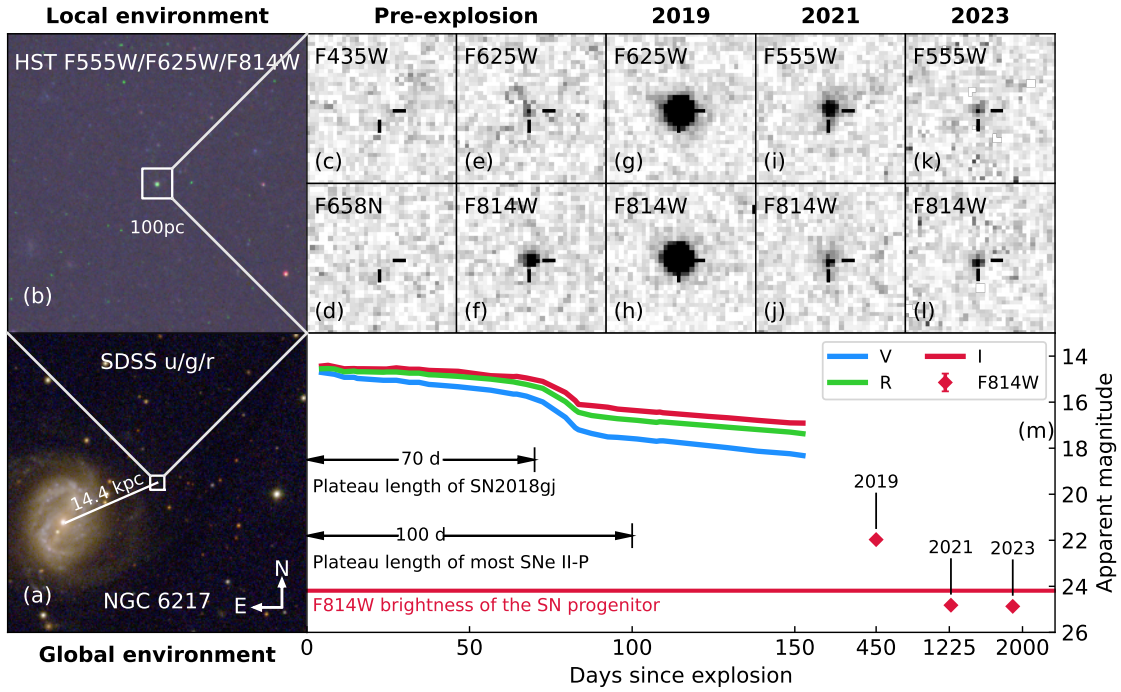


Fig. 1: Direct pre-explosion detection of SN 2018gj's progenitor and the photometric evolution of SN 2018gj. (a) SDSS  $u/g/r$  composite image of NGC 6217, where SN 2018gj is located in the far outskirt. (b) HST F555W/F625W/F814W composite image of the local SN environment, which is a very sparse region without any prominent features of recent star formation. (c–l) HST images taken before and after the explosion of SN 2018gj. The crosshairs indicate the SN position. (m) Light curves of SN 2018gj from the literature [33] and late-time photometry from the HST observations. SN 2018gj has a very short plateau length of 70 days in contrast to 100 days for most SNe II-P. In 2021 and 2023, the F814W brightness becomes much fainter than the pre-explosion level, suggesting that the SN progenitor has disappeared after explosion.

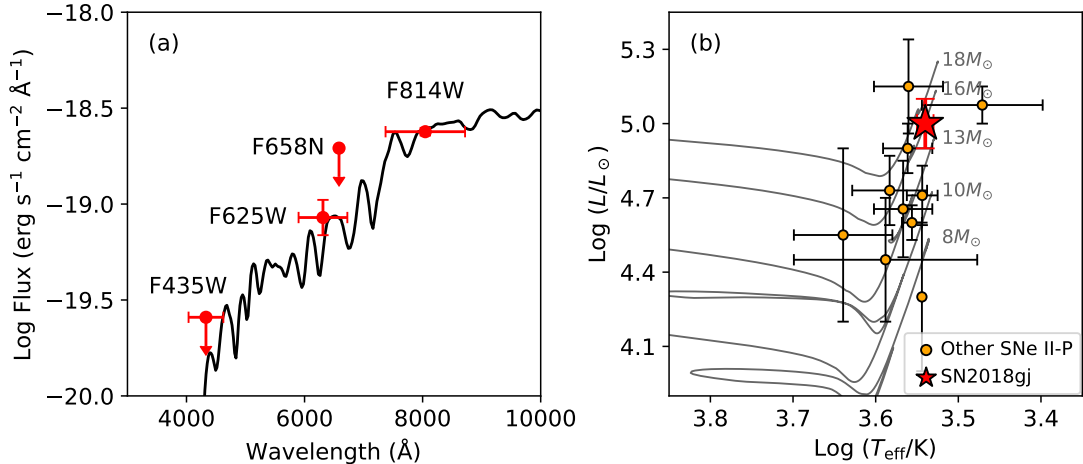


Fig. 2: Progenitor properties derived from the direct detections. (a) SED of the SN progenitor and the best-fitting MARCS [38] theoretical spectrum, consistent with being a luminous RSG. (b) Position of SN 2018gj's progenitor on the HRD in comparison with other confirmed SNe II-P progenitors and the BPASS [39] single-star evolutionary tracks for solar metallicity.

tive observational characteristics. (1) In contrast to most core-collapse SNe that are associated with active star-forming regions, SN 2018gj is located in a very sparse area as far as 14.4 kpc from the host-galaxy center and without any obvious signs of recent star formation. (2) While

the peak luminosity, color, and spectral evolution are all typical for SNe II-P, SN 2018gj displays a remarkably short plateau of only  $70 \pm 2$  days [33] compared with an average plateau length of  $\sim 100 \pm 20$  days for most SNe II-P [51, 52] (Fig. 1m). In this section, we shall investigate

TABLE 1: HST observations and photometry of SN 2018gj.

Date	Epoch <sup>a</sup> (day)	Instrument	Filter	Exposure Program		Magnitude <sup>c</sup> (mag)
				Time (s)	ID	
2009-06-13	-3133	ACS/WFC	F435W	500 <sup>b</sup>	11371	>28.5
2009-06-13	-3133	ACS/WFC	F625W	400 <sup>b</sup>	11371	26.10 (0.23)
2009-07-08	-3108	ACS/WFC	F658N	500 <sup>b</sup>	11371	>24.9
2009-07-08	-3108	ACS/WFC	F814W	400 <sup>b</sup>	11371	24.19 (0.05)
2019-05-16	491	WFC3/UVIS	F625W	1305	15151	22.51 (0.01)
2019-05-16	491	WFC3/UVIS	F814W	1305	15151	21.97 (0.02)
2021-06-27	1264	WFC3/UVIS	F555W	710	16179	25.07 (0.06)
2021-06-27	1264	WFC3/UVIS	F814W	780	16179	24.82 (0.09)
2023-02-27	1874	ACS/WFC	F555W	760	17070	25.91 (0.18)
2023-02-27	1874	ACS/WFC	F814W	780	17070	24.87 (0.07)

<sup>a</sup> Relative to an estimated explosion date of 2018-04-10 [33].

<sup>b</sup> The effective exposure time of these observations, as listed here, is half of the total exposure time since the SN position is covered by only one of the two dithered exposures.

<sup>c</sup> All magnitudes reported in this paper are in the Vega magnitude system.

the origin of SN 2018gj based on the direct progenitor detection combined with these two characteristics.

### A. Environment and age

We analyzed the environment of SN 2018gj with the surrounding stellar populations detected on the post-explosion HST/WFC3 images, which have a better spatial resolution and deeper detection limits than those acquired by ACS. In each band (F555W, F625W and F814W), we considered a star to be significantly detected if the parameters reported by DOLPHOT met the following criteria:

- type of source, **TYPE** = 1;
- signal-to-noise ratio, **SNR**  $\geq 3$ ;
- photometry quality flag, **FLAG**  $\leq 2$ ;
- source sharpness,  $-0.5 < \text{SHARPNESS} < 0.5$ ;
- source crowding, **CROWDING**  $< 1$ .

These criteria excluded bad detections, extended sources and cosmic-ray residuals, leaving only well-measured point sources. We also used artificial star tests to estimate the detection limit in each band; an artificial star was considered to be successfully recovered if it was found within 1 pixel of the inserted position and its DOLPHOT parameters met all the above criteria. The detection limit in a filter was characterized by  $m^{\text{lim}} \pm \sigma_m^{\text{lim}}$ , where  $m^{\text{lim}}$  is the magnitude where the detection probability falls to 50% and  $\sigma_m^{\text{lim}}$  is its “uncertainty”, i.e. the magnitude range where the recovery rate declines from 68% to 32%.

Fig. 3a shows the map of stars detected in the SN vicinity. It is obvious that SN 2018gj is located in a very sparse

region with a very uniform stellar distribution, except for a stellar surface over-density to its northwest. This over-density may arise from the random Poisson noise of a uniform distribution; it is also possible that the over-density is the relic of an old star-forming complex that has almost dispersed. We define a small circular region with a radius of 380 pc covering the over-density (dashed circle, hereafter  $R_{\text{od}}$ ); we also define a large circular region with a radius of 850 pc centered on the SN position and encompassing the over-density (solid circle, hereafter  $R_{\text{env}}$ ). There are 131 sources within the  $R_{\text{env}}$  region and 42 sources inside the  $R_{\text{od}}$  region. Their Color-magnitude diagrams (CMDs) are shown in Fig. 3c and d. There is no significant difference between those inside and outside the overdensity. This suggests that the over-density stars should have very similar ages to the other stars in the SN vicinity.

We use stars within the above-defined  $R_{\text{env}}$  region to derive the stellar age distribution in the SN environment. This is performed by fitting their CMDs with a hierarchical Bayesian approach [53, 54] as detailed in the Supplementary Materials. The derived stellar age distribution is shown in Fig. 3b and the best-fitting model CMDs are displayed in Fig. 3c and d. Most stars were formed at  $\log(t/\text{yr}) \geq 7.60 \pm 0.05$  and very few, if any, were formed at  $\log(t/\text{yr}) = 7.1\text{--}7.3$ , the progenitor age of SN 2018gj expected from single-star evolution.

In previous studies, much smaller regions (i.e. 100–200 pc, [18, 53]) were usually used to study SN environments such that stars within the regions are coeval with the SN progenitor and an accurate age can be derived for the progenitor. For SN 2018gj, however, using a large region should not be a problem since we only found a lower age limit for the SN progenitor – if there are no young stars within 850 pc, there are no young stars within 100–200 pc. Besides, as discussed above, this region is very

sparse and uniform, without obvious age variation between different positions. This is not like the young star-forming regions with high spatial variations. Therefore, the defined  $R_{\text{env}}$  region is representative for the environment of SN 2018gj. We have also conducted tests using 28 sources within 400 pc, and the fitted stellar age distribution does not change significantly except for larger uncertainties. Using a large region can include a larger number of stars and reduce the random errors in the derived stellar age distribution.

It is also worth mentioning that the defined region is large enough to include the birthplace of the progenitor even if it is a walkaway or runaway star ejected from a prior binary system, which can travel an average distance of  $\sim 100$  pc during its short lifetimes [55, 56]. The birthplace may lie outside the defined region if the progenitor was a hypervelocity star ejected from the host galaxy's center. However, we deem this scenario highly unlikely due to the low ejection rate [57, 58]. Moreover, given the distance to the galactic center and the lifetime of a single star with  $M_{\text{He}} = 4.6 \pm 0.7 M_{\odot}$ , even under an extreme ejected velocity of 1000 km s $^{-1}$ , the progenitor would need to have been ejected very early during its main sequence (MS), when the progenitor was compact and had low mass-loss rate. This is in contradiction to the low-mass H-rich envelope for SN 2018gj (see below).

The above analysis is based on the stellar population around the SN. The possibility of an underlying stellar cluster at the SN position can be ruled out. Given the deep detection limit in the F435W band on the pre-explosion image, the initial mass of any potential stellar cluster younger than 50 Myr (the lifetime of a  $8 M_{\odot}$  star) would be less than  $50 M_{\odot}$ . However, such a very low-mass cluster is expected to host only 0.04 massive stars. Therefore, it is very unlikely that the progenitor of SN 2018gj is associated with a star cluster at the SN position.

## B. Light curve and final H-envelope mass

The short plateau length in the light curve points to an abnormally low-mass H-rich envelope for the progenitor of SN 2018gj. Ref. [33] estimated the final H-envelope mass by carrying out hydrodynamical modelling with MESA [59] and STELLA [60] (their Section 5). They tried two sets of models with progenitor initial masses of  $M_{\text{ini}} = 13 M_{\odot}$  and  $19 M_{\odot}$ , respectively, and changed the final H-envelope mass by arbitrarily tuning the wind mass-loss rate. They found that the pseudo-bolometric light curve and the Fe II  $\lambda 5169$  Å velocity evolution can be fitted with an explosion energy of  $4 \times 10^{50}$  erg, an initial progenitor mass of  $M_{\text{ini}} = 13 M_{\odot}$  and a final H-envelope mass of  $M_{\text{H}} = 3.26 M_{\odot}$  which was achieved by increasing the default wind mass-loss rate by a factor of 5.

We also carried out a similar analysis by employing

MESA code (version 15140) for an initial progenitor mass of  $M_{\text{ini}} = 15 M_{\odot}$  (based on the MESA test suite 15M.dynamo), which is more consistent with our progenitor detection. We show models with different final H-envelope masses in the Supplementary materials. The best-fitting model has a final H-envelope mass of  $M_{\text{H}} = 3.5 \pm 0.5 M_{\odot}$ , achieved by scaling the default wind mass-loss rate by a factor of 3.0–3.5. This final H-envelope mass is adopted for further analysis in this work. It is very similar to that of [33], which is reasonable since the SN light curve shape is very sensitive to H-rich envelope but depends very little on the He-core mass [61].

Interaction between the SN ejecta and circumstellar material (CSM) may affect the light curve and cause uncertainties in measuring the final H-envelope mass [62, 63]. For SN 2018gj, no narrow emission lines from ejecta-CSM interaction can be seen in the spectra [33]. In Ref. [33], a CSM of  $< 0.15 M_{\odot}$  was incorporated to fit the early pre-peak light curve. However, this CSM mass is very small and has very little effect on the plateau after peak. Therefore, the possible effect of CSM on measuring the final H-envelope mass can be neglected.

In addition, a recent study by Ref. [64] presents scaling relations between SN observables and progenitor properties, considering the partial stripping of the H-rich envelope. Degeneracies in the scaling relations can be further broken [65] given the progenitor radius ( $875 \pm 140 R_{\odot}$ , inferred in this work),  $^{56}\text{Ni}$  mass from the light-curve tail ( $0.025\text{--}0.03 M_{\odot}$ , [33]), and explosion energy from the bolometric light curve and Fe II  $\lambda 5169$  Å velocity evolution ( $4 \times 10^{50}$  erg, [33]). With these parameters, the plateau length corresponds to a final H-envelope mass of  $M_{\text{H}} = 3.00\text{--}3.68 M_{\odot}$  based on the scaling relations. This is also consistent with our derived value.

We notice that Ref. [66] presented a different hydrodynamical modelling and derived a significantly larger SN ejecta mass of  $23 M_{\odot}$ , corresponding to an initial progenitor mass of  $29 M_{\odot}$ . Their results are significantly larger than that inferred from SN nebular spectroscopy and direct detection of the progenitor. Furthermore, the explodability of such a massive progenitor also warrants consideration [67]; even if such a star were to explode, it would manifest itself as a H-poor SN rather than a H-rich SN due to its powerful stellar winds (e.g., Refs. [68, 69]).

## C. Evidence for binary origin

With the final He-core mass, final H-envelope mass and environment-based age constraint, we were able to determine whether a binary progenitor is more favored than a single-star progenitor for SN 2018gj. This is achieved by comparing the observables with theoretically predicted values for single and binary progenitors (Fig. 4). For the single progenitors, we show the models from BINARY-C, POSYNDON or BPASS while for the binary progenitors we

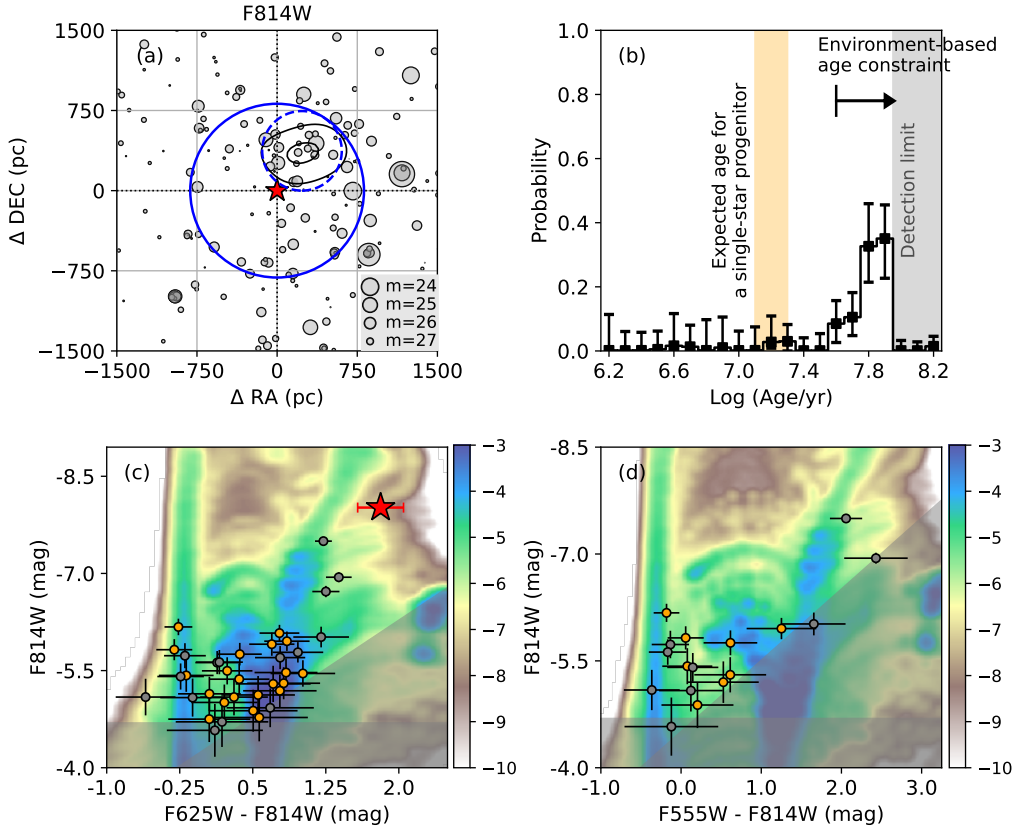


Fig. 3: Estimation of the stellar age for SN 2018gj’s progenitor. (a) Map of stars detected on the HST/WFC3/F814W images in the environment of SN 2018gj with the symbol size reflecting their magnitudes. (b) The stellar age distribution in the SN local environment derived from the CMD fitting. (c,d) CMD of the resolved stellar populations inside the  $R_{od}$  region (gray) and inside the  $R_{env}$  region but outside the  $R_{od}$  region (orange) in comparison with the SN progenitor (red point). The error bars are the photometric uncertainties and the grey-shaded area corresponds to the detection limits. The background color scale shows the normalized probability density distribution for the environmental sources simulated with the BPASS binary population models.

show the results from the BINARY\\_C population synthesis [29, 40, 70–72]. While BINARY\\_C has a limited accuracy based on analytical formulae of pre-computed single stellar models, it has the advantage of being able to rapidly calculate all possible binary scenarios and their contribution in a homogeneous way, implementing a large number of binary models on a dense grid of parameters that have already been tested in previous dedicated studies on the age and pre-SN properties of binary SN progenitors [14, 22, 29, 30].

As shown in Fig. 4, SN 2018gj’s progenitor is a clear outlier from single-star models (be it BINARY\\_C, POSYNDON or BPASS). Assuming a single star, the progenitor should have an initial mass of  $M_{ini} = 13\text{--}16 M_{\odot}$  and an age of  $\log(t/\text{yr}) = 7.1\text{--}7.3$ . The environment of

SN 2018gj, however, is old and sparse, where most stars were formed at  $\log(t/\text{yr}) \geq 7.60 \pm 0.05$ . Moreover, the progenitor has an abnormally low final H-envelope mass of only  $M_H = 3\text{--}4 M_{\odot}$  while those for most SNe II-P lie in the range of  $M_H \sim 6\text{--}8 M_{\odot}$  [64]. Given that the (single-star equivalent) progenitor mass and the roughly solar metallicity of SN 2018gj are quite normal for SNe II-P [5], the stripped envelope is very unlikely to be a consequence of a mass- and metallicity-dependent wind in single-star evolution.

Quantitatively, we use a statistical Bayesian approach to distinguish single-star and interacting-binary progenitor channels. This can be regarded as a model-selection

problem, in which

$$\frac{P(\text{BIN}|D)}{P(\text{SIN}|D)} = \frac{P(D|\text{BIN})}{P(D|\text{SIN})} \frac{P(\text{BIN})}{P(\text{SIN})}, \quad (2)$$

where  $D = (M_{\text{H}}, M_{\text{He}}, \log(t))$  is the observable,  $P(\text{BIN})$  and  $P(\text{SIN})$  are the prior probabilities for the single and binary progenitor models,  $P(\text{BIN}|D)$  and  $P(\text{SIN}|D)$  are the posterior probabilities for the models given the observational data. The ratio of the posterior is the prior odds multiplied by the ratio of the evidence; the latter quantity is also regarded as the Bayes factor (BF) in favor of binary-progenitor model. Population synthesis has predicted that roughly 30–50% of Type II SNe progenitors have a history of binary interaction (i.e. [10, 22, 25]), and we conservatively apply theoretical priors of  $P(\text{BIN}) = 0.4$  and  $P(\text{SIN}) = 0.6$ . In this case,

$$P_{\text{BIN}} = \frac{2 \times \text{BF}}{3 + 2 \times \text{BF}} \quad (3)$$

describes the relative probability of binary-progenitor model.

The Bayesian model evidences,  $P(D|\text{mod})$  with mod = SIN or BIN, can be calculated by marginalizing the model parameters:

$$P(D|\text{mod}) = \int p(D|\theta, \text{mod})p(\theta|\text{mod})d\theta, \quad (4)$$

where  $\theta = M_1$  (i.e. stellar initial mass) or  $(M_1, M_2, P)$  (i.e. the initial primary mass, secondary mass and binary orbital period) in the single and binary progenitor models, respectively.  $p(\theta|\text{mod})$  is the prior probability distribution for the model parameters and  $p(D|\theta, \text{mod})$  is the likelihood. Given  $\theta$ , BINARY\_C has already synthesized a large population of single and binary SN progenitors with predicted properties of  $\mu = (M_{\text{H}}^{\text{mod}}, M_{\text{He}}^{\text{mod}}, \log(t)^{\text{mod}})$ . Therefore, Eq. (4) is equivalent to:

$$P(D|\text{mod}) = \sum_i^{N_{\text{mod}}} p_i \times P(D|\text{mod}_i), \quad (5)$$

where  $\text{mod}_i$  is the  $i$ -th model and  $p_i$  is its weight in the synthesized population. The  $i$ -th model has predicted values of  $\mu_i = (M_{\text{H},i}^{\text{mod}}, M_{\text{He},i}^{\text{mod}}, \log(t_i)^{\text{mod}})$ .

With the derived values of  $M_{\text{H}}$  and  $M_{\text{He}}$  and the environment-based age constraint for SN 2018gj, Eq. (5) can be further expressed as:

$$P(D|\text{mod}) = \sum_i^{N_{\text{mod}}} p_i \times \left[ \sum_k^{N_{\text{pop}}} w_k \times P(D_k|\text{mod}_i) \right], \quad (6)$$

where  $w_k$  is the weight of the  $k$ -th model population and  $D_k = (M_{\text{H}}, M_{\text{He}}, \log(t_k))$  with  $\log(t_k)$  being the age of this population (see Section III A). We use Gaussian likelihood for  $P(D_k|\text{mod}_i)$ :

$$p(D_k|\text{mod}_i) = (2\pi)^{-3/2} |\Sigma|^{-1/2} \times \exp \left[ -\frac{1}{2} (D_k - \mu_i)^T \Sigma^{-1} (D_k - \mu_i) \right]. \quad (7)$$

We consider both the measurement and model uncertainties of the three observables and the error covariance matrix takes the form

$$\Sigma = \begin{bmatrix} \sigma_{M_{\text{H},\text{obs}}}^2 & 0 & 0 \\ 0 & \sigma_{M_{\text{He},\text{obs}}}^2 & 0 \\ 0 & 0 & \sigma_{\log(t),\text{obs}}^2 \end{bmatrix} + \begin{bmatrix} \sigma_{M_{\text{H},\text{mod}}}^2 & 0 & 0 \\ 0 & \sigma_{M_{\text{He},\text{mod}}}^2 & \rho \sigma_{M_{\text{He},\text{mod}}} \sigma_{\log(t),\text{mod}} \\ 0 & \rho \sigma_{M_{\text{He},\text{mod}}} \sigma_{\log(t),\text{mod}} & \sigma_{\log(t),\text{mod}}^2 \end{bmatrix}. \quad (8)$$

The former term in Eq. (8) corresponds to the measurement uncertainties, in which we use half of the age bin size (i.e. 0.05 dex) as the measurement uncertainty for  $\sigma_{\log(t),\text{obs}}$ . The latter term corresponds to the model uncertainties. The uncertainty of the final H-envelope mass was adopted as  $\sigma_{M_{\text{H},\text{mod}}} = 20\% M_{\text{H},\text{mod}}$ , primarily due to the highly uncertain mass-loss prescriptions especially during the RSG phase [73, 74]. This can be also observed from the discontinuity of  $M_{\text{H}}$  for the single-star track at  $M_{\text{He}} = 4 M_{\odot}$  (Fig. 4b), which is due to different mass-loss prescriptions used for different progenitor mass regimes. Material mixing induced by stellar rotation and convective overshooting can transport the H-rich material from the envelope to the core; this process adds new fuel for nuclear burning and results in larger final He-core mass and longer stellar lifetime [67, 75, 76]. For the uncertainty in the final He-core mass, we used the difference between typical assumptions in convective core overshooting such as the assumption in Ref. [77] (implemented in POSYDON and calibrated for massive stars) and of lower values implemented in the models of BINARY\_C [78], which is potentially more relevant for low-mass stars. This yields  $\sigma_{M_{\text{He},\text{mod}}} = 1 M_{\odot}$  for stars with  $M_{\text{ini}} = 12\text{--}15 M_{\odot}$ , corresponding to the single-star equivalent initial mass for SN 2018gj and typical of Type II SN progenitors. Meanwhile, rotation can extend the MS lifetime by approximately 20% [75] for stars with  $M_{\text{ini}} \gtrsim 7 M_{\odot}$ ; we therefore adopted  $\sigma_{\log(t),\text{mod}} = \log_{10}(1.2t) - \log_{10}(t) \approx 0.08 \text{ dex}$  on a log scale.

In the error covariance matrix (Eq. (8)) we introduce a correlation coefficient  $\rho$  between the model uncertainties of final He-core mass and age. The  $\rho$  should be positive and relatively large, as both parameters are affected simultaneously by the same source of error (i.e. chemical mixing). For example, the impact of convective uncertainties on stellar structure and evolution was explored by varying relevant parameters [76]. The correlation coefficient of the resulting He-core mass and stellar lifetime (their Table 1) is 0.90 for the  $M_{\text{ini}} = 15 M_{\odot}$  star. We note, however, that both quantities may also be affected by other physical processes, such as rotation, at the same time. Besides, we assume no correlation between the model uncertainty of final H-envelope mass and that of any other parameter, since its uncertainty is

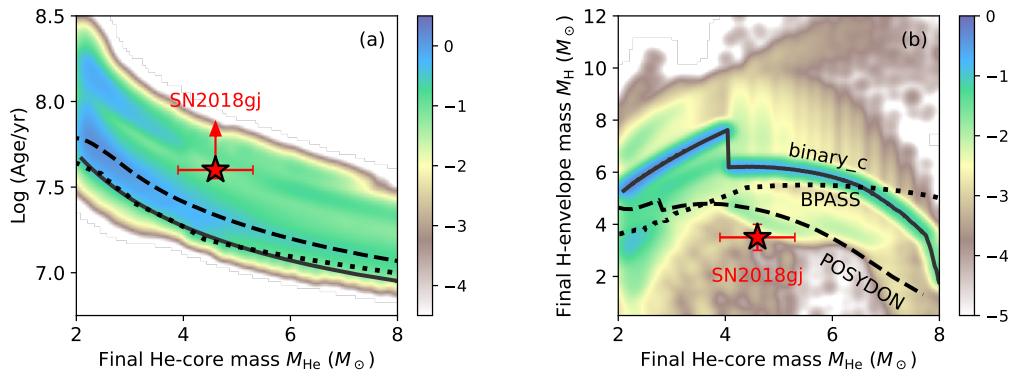


Fig. 4: Final He-core mass ( $M_{\text{He}}$ ), final H-envelope mass ( $M_{\text{H}}$ ) and age of SN 2018gj’s progenitor. For comparison, the solid/dotted/dashed black lines show the relations between the parameters for single-star progenitors from BINARY\_C/BPASS/POSYDON and the color scales show the probability density distributions for binary progenitors as predicted by BINARY\_C [29]. The probability densities are on logarithmic scales and the color bars are in units of  $M_{\odot}^{-2}$  (panel a) or  $M_{\odot}^{-1} \text{dex}^{-1}$  (panel b).

dominated by another source of error (i.e. the mass-loss prescriptions), with negligible influences from variations in stellar structures.

With the above method we find the binary-progenitor probability,  $P_{\text{BIN}}$ , should be very close to 1. While  $P_{\text{BIN}}$  increases as  $\rho$  approaches 1, it remains insensitive to the value of  $\rho$ ; specifically, it remains greater than 99% even when  $\rho$  is reduced to 0.2. In the unphysical scenario where  $\rho$  becomes as low as 0.1 or 0.0,  $P_{\text{BIN}}$  only decreases to 88% or 68%, respectively. Moreover, if a slightly higher prior has been used (i.e.  $P(\text{BIN}) = P(\text{SIN}) = 0.5$ , as in [31]; essentially being agnostic to the expected occurrence of progenitors with binary history), the resulting posterior  $P_{\text{BIN}}$  increases to 91% and 76% for  $\rho = 0.1$  and 0.0, further supporting the robustness of the binary origin.

Note that the stellar age distribution in the environment of SN 2018gj has a non-negligible error, including that at the progenitor age expected from single-star evolution (i.e.  $\log(t/\text{yr}) = 7.1\text{--}7.3$ ). We repeated the calculation by adopting  $w_k$  from the last 1000 walkers to account for this uncertainty. In all cases,  $P_{\text{BIN}}$  remains almost unchanged. Therefore, our result robustly establishes SN 2018gj as arising from an interacting binary progenitor.

The estimated lower limit of the final He-core mass of SN 2018gj,  $M_{\text{He}} \approx 3.2 M_{\odot}$ , in case of high variability due to pulsations (Sec. II), would still be only barely consistent with the ages expected from single-star models assuming high mixing, such as in POSYDON (dashed line in Fig. 4). Moreover, this lower mass estimate would be in tension with the progenitor mass independently inferred from nebular spectroscopy [33]. Although the explosion phase within a pulsation cycle can change the decline rate of the plateau in optical light curves, it does not effectively affect the plateau duration and decay tail [46]. After accounting for radial pulsations as demonstrated in [46], and applying the same scaling relation, we find

that the resulting variation in the final H-envelope mass is negligible to the current observational uncertainties. Consequently, we argue that the evidence supporting a binary progenitor for SN 2018gj remains robust against the effects of large-amplitude pulsations.

#### IV. MODELLING PRE-SUPERNOVA EVOLUTION

In order to better understand the progenitor of SN 2018gj, we perform a detailed modelling of binary systems that can give rise to such an event. In this investigation, we use the next-generation binary population synthesis framework, POSYDON (v2) [42] (expanding its previous public version [41]), which is based on extended grids of detailed binary systems with MESA [59, 79–82]. These detailed binary models are crucial to follow accurately the response of both stars during multiple episodes of binary mass transfer, including the reverse mass transfer phases and eventual merger that are found to be important for this progenitor. POSYDON also provides self-consistent treatment of tidal evolution, contact phases, and rotation in its dense binary grids. For binaries with a non-degenerate accretor, initially all the material transferred by the donor through Roche-lobe overflow (RLOF) is accepted by the gainer and the accretion is restricted when the spun-up mass gainer reaches its critical rotation. For the common envelope (CE) evolution, we assume an efficiency of  $\alpha_{\text{CE}} = 1$  in the  $\alpha\text{-}\lambda$  formalism [83, 84] and calculate the binding energy parameter  $\lambda$  based on the detailed stellar profile of the donor star when the CE is triggered. All massive progenitors reach up to carbon core depletion, which is only decades away from core collapse. We exclude core-collapse progenitors that are expected to implode to black holes without a transient event according to [85] mapping to the pre-SN

state and [86] explodability criterion.

In this framework<sup>3</sup>, we conduct a comprehensive search of the binary parameter space for models that reproduce the empirical values of the core mass, age, and envelope mass of the SN 2018gj progenitor, within its observational errorbars as discussed in Sections II and III A. We use a primary initial mass range of  $M_1 = 5\text{--}250 M_\odot$ , a flat initial secondary-to-primary mass ratio distribution from 0.05 to 0.99, and an initial period distribution following [9] between 0.75 and 3500 days. We assume solar metallicity for simplicity, as in all our analysis in this study (although see the Supplementary materials). We evolved  $5 \times 10^4$  systems on the parameter grids, performing an initial-final linear interpolation for the computed final properties of the binary models.

Although binary scenarios including MS+MS mergers are found in principle to be able to produce a high mass core at longer delay-times, they have been excluded from our analysis as they are assumed to form a stellar structure similar to a more massive MS star, without being able to reproduce the uncommon core-to-envelope mass ratio. Similarly, scenarios involving the merging of an evolved giant star with a MS companion, although allowed, are found not to reproduce the long inferred age of the SN event. Thus, we find reverse merger scenario to be the main route towards a SN 2018gj-like progenitor, plausibly reproducing all of its empirical values.

The full evolution of an example reverse merger system, plausible for the evolution of SN 2018gj progenitor, is shown in Fig. 5. The initial masses of the stellar components in the binary system ( $\lesssim 9M_\odot$ ) are the reason of the long-delay time until collapse. Although we consider the binary's evolution modeled with MESA binary systems until merging quite reliable, the merger product's subsequent evolution is more simplified (gray region in Fig. 5b) but can still lead to physically-motivated conclusions. To more accurately estimate the eventual explodability of the merger product, we match the merger product with a single star model, whose He-core mass (if already formed during the evolution for both stars), CO-core mass, and mass-weighted average central He abundance are as similar as possible to the new cores of the merger product. The merging of the two formed cores of the evolved stars enables a high core mass at such a long age. At the same time, as the mass loss during a merger involving two evolved stars is highly uncertain, we consider a range of post-merger envelope masses between two assumptions: on one hand the conservative merger scenario (shown in the top of the star-hashed total mass of Fig. 5b); on the other hand, the expected mass loss from unbinding of part of the donor's pre-CE envelope corresponding to the orbital energy released during spiraling-in at the CE phase [87]. A partial mass loss within this range can explain the low-mass envelope of

SN 2018gj. Although in principle a non-conservative CE phase can form CSM around the merger product as seen in SN 2018gj, we do not expect this to be present until explosion, after  $\sim 1$  Myr in our example system (although the CSM may be the indirect outcome of a different evolution of a merger product until explosion, compared to single stars).

The initial parameter space of binary systems that undergo a reverse merger and evolve towards a SN 2018gj-like progenitor is shown in Fig. S2 (online). Such systems have a relatively low initial primary mass of  $M_1 = 8.3\text{--}9.3 M_\odot$ , an almost equal initial mass ratio of  $q = 0.85\text{--}0.97$ , and a short initial period of  $P = 3.0\text{--}6.5$  days. Binaries of slightly lower initial mass ratios do not lead to unstable reverse mass transfer, whereas wider systems start their first mass transfer not during but after the MS phase of the primary, resulting in SN progenitors inconsistent with that of SN 2018gj.

Binary channels involving these kind of reverse mergers have been suggested to give rise to SN progenitors with long delay times. If the initial mass of the primary star is below the minimum mass threshold of  $\sim 8 M_\odot$  for core-collapse SNe, these merger SN progenitors can exceed the lifetimes of all SNe originating from single-stars [22, 29]. There has been observational evidence of SN remnants [29, 88] and compact object remnants [89] that their inferred age favor scenarios of prior mass exchange or merging in a binary system, potentially reverse merging. Additionally, there are indications, although inconclusive, of prolonged SN ages [90]. The scenario discussed here for SN 2018gj can be seen as a slightly higher mass analog of the current state and expected outcome of the  $\phi$  Persei system [91]. Similar scenarios of reverse mergers involving two already-formed cores can lead to merger products with high angular momentum budget within their cores, suggested as potential channel for long gamma-ray bursts [92, 93].

## V. CONCLUSION

SNe II-P are the most common type of core-collapse SNe in the local Universe and play critical roles in many aspects of astrophysics. Since decades ago theorists have predicted that they may originate not only from single stars but also from interacting binaries; however, robust observational evidence still remains elusive for this speculated binary progenitor channel.

In this paper, we report the first identification of a SN II-P progenitor with compelling evidence of binary origin in the case of SN 2018gj. The progenitor is detected on the pre-explosion HST images and has disappeared after explosion. The progenitor has an effective temperature of  $\log(T_{\text{eff}}/\text{K}) = 3.54 \pm 0.01$ , a luminosity of  $\log(L/L_\odot) = 5.0 \pm 0.1$  and a final He-core mass of  $M_{\text{He}} = 4.6 \pm 0.7 M_\odot$ .

While the directly detected progenitor exhibits deceptively typical temperature and luminosity of other SN II-

<sup>3</sup> Exact POSYDON commit used in this work is [891c5897](#).

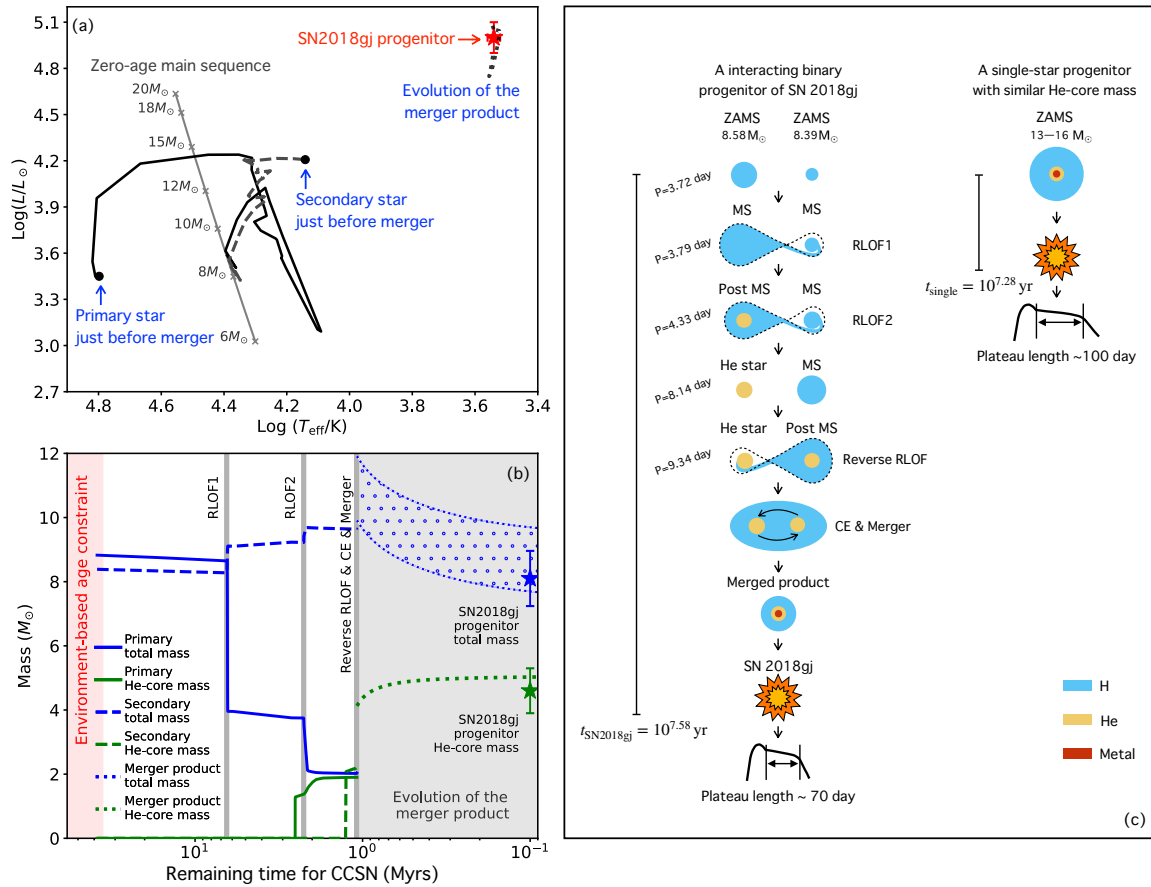


Fig. 5: Pre-supernova evolution simulated with POSYDON. (a) Pre-SN evolution of the progenitor system of SN 2018gj on the HRD. (b) Evolution of the total stellar mass and He-core mass of the primary star, secondary star, and merger product before explosion. Episodes of mass transfer are labeled in vertical, which are self-explanatory. The blue dotted region reflects the uncertainty of the total mass of the merger product with upper/lower limit corresponding to a conservative merging/partial CE ejection. Evolution continues up to core carbon depletion, expected to occur less than thousands of years before core collapse, with no significant further change in stellar mass or position on the HRD. (c) A schematic plot of the pre-SN evolution.

P progenitors, it is located in an unexpectedly old environment, with age of  $\log(t/\text{yr}) \geq 7.6 \pm 0.05$ , and displays an abnormally short plateau in the light curve, which corresponds to a very low final H-envelope mass of  $M_H = 3.5 \pm 0.5 M_\odot$ . Both phenomena are inconsistent with expectations from single-star evolution, and we show that SN 2018gj is unambiguously associated with a binary progenitor with a high probability of  $> 99\%$ .

With state-of-the-art binary simulation code POSYDON we further reveal the initial parameters and the pre-SN evolution of the progenitor system of SN 2018gj. The system is found to be initially a close binary consisting of two nearly equal-mass stars with primary mass  $M_1 = 8.3\text{--}9.3 M_\odot$ , secondary-to-primary mass ratio  $q = 0.85\text{--}0.97$  and period  $P = 3.0\text{--}6.5$  days. The system experienced a reverse merger scenario, which involves a complicated history of mass transfer back and forth between the two stars followed by a merger. The merger product corresponds to the direct progenitor of SN 2018gj that we have detected on the pre-explosion image, and this

scenario explains all the observational characteristics.

This study provides the first robust observational evidence for the long-sought interacting binary progenitor channel toward SNe II-P, which is key to decipher the origin of this major class of SNe as well as their observational diversity. Our study also establishes a successful methodology that can motivate future investigations to uncover a previously hidden population of SNe II-P from binaries in the wealth of data of existing and upcoming surveys such as CSST, Euclid, Roman, ZTF and LSST.

## Acknowledgments

This work is supported by the Strategic Priority Research Program of the Chinese Academy of Sciences (XDB0550300), the National Natural Science Foundation of China (12303039, 12303051, 12261141690, and

12588202). EZ and DS acknowledge support from the Hellenic Foundation for Research and Innovation (H.F.R.I.) under the “3rd Call for H.F.R.I. Research Projects to support Post-Doctoral Researchers” (7933). EZ acknowledges useful discussion with Azalee Bostroem, Jared Goldberg and Natalia Ivanova. JJA acknowledges support provided through a grant (JWST-AR-04369.001-A) from the STScI under NASA contract NAS5-03127. MMB was supported by the Boninchi Foundation, the Swiss National Science Foundation (CRSII5.21349), and the Swiss Government Excellence Scholarship. MF is supported by a Royal Society - Science Foundation Ireland University Research Fellowship. MK was supported by the Swiss National Science Foundation Professorship grant (PI Fragos, PP00P2 176868). SG, CL, PMS and ET were supported by the Gordon and Betty Moore Foundation (PI Kalogera, GBMF8477 and GBMF12341). ZWL work is supported by the National Natural Science Foundation of China (12288102), the Strategic Pri-

ority Research Program of the Chinese Academy of Sciences (XDB1160303), the International Centre of Supernovae (ICESUN), Yunnan Key Laboratory of Supernova Research (202302AN360001) and the Yunnan Revitalization Talent Support Program “YunLing Scholar” project. YY’s research is partially supported by the Tsinghua University Dushi Program. JFL acknowledges support from the New Cornerstone Science Foundation through the New Cornerstone Investigator Program and the XPLOTER PRIZE.

This research is based on observations made with the NASA/ESA Hubble Space Telescope obtained from the Space Telescope Science Institute, which is operated by the Association of Universities for Research in Astronomy, Inc., under NASA contract NAS 5-26555. This work made use of v2.2 of the Binary Population and Spectral Synthesis (BPASS) models as described in [39] and [94].

## Appendix A: Distance, reddening and metallicity

SN 2018gj occurred in the nearby galaxy NGC 6217 with a heliocentric redshift of  $z = 0.004540$  (from [95] and the NASA/IPAC Extragalactic Database). This corresponds to a cosmic-expansion velocity of  $1774 \pm 18 \text{ km s}^{-1}$ , which has been corrected for the influence of the Virgo cluster, Great Attractor and Shapley supercluster [96]. Adopting a Hubble constant ( $H_0$ ) of  $73.30 \pm 1.04 \text{ km s}^{-1} \text{ Mpc}^{-1}$  [97], the distance to NGC 6217 was estimated to be  $24.2 \pm 0.4 \text{ Mpc}$  and this value was used throughout this paper.

SN 2018gj has a total line-of-sight reddening of  $E(B - V) = 0.08 \pm 0.02 \text{ mag}$ , consisting of a Galactic reddening of  $E(B - V) = 0.04 \text{ mag}$  from the IRSA-Galactic Dust Reddening and Extinction map [98] and a host-galaxy reddening of  $E(B - V) = 0.04 \pm 0.02 \text{ mag}$  as estimated with the Na I D absorption feature in the SN spectra [33]. Given the very low value of reddening, variation of the extinction law has a very small influence on our results and we used a standard Galactic extinction law with  $R_V = 3.1$  [99] in this work.

NGC 6217 is a nearly face-on, Seyfert 2 disk galaxy with a total mass of about  $10^{10.8} M_\odot$  and a high metallicity of  $12 + \log(\text{O/H}) = 8.98$  near the center [100, 101]. The metallicities for disk galaxies decrease outward and, for massive galaxies of  $> 10^{10.5} M_\odot$ , the metallicity gradients are very similar to each other [102]. Therefore, we used the metallicity gradient of  $-0.020 \pm 0.006 \text{ dex kpc}^{-1}$  of M81, which is also a massive Seyfert 2 galaxy and resembles NGC 6217 very much in the morphology, as an estimate of that for NGC 6217 [103]. This corresponds to a solar metallicity at the position of SN 2018gj. In addition, Ref. [33] found that the evolution of  $\text{Fe II} \lambda 5169 \text{ \AA}$  pseudo-equivalent width of SN 2018gj is consistent with hydrodynamical models with solar or half-solar metallicities. Combining these estimates, we adopted a solar metallicity for SN 2018gj in the whole analysis. It is worth mentioning that the conclusion of this paper will not be affected even if SN 2018gj has a sub-solar metallicity, where if anything, lower wind mass-loss rates [104, 105] and less efficient Roche-lobe stripping [106, 107] are expected.

## Appendix B: Fitting for the star formation history

In order to derive the stellar age distribution of the SN environment, we fit stars inside the large circular region,  $R_{\text{env}}$ , with model stellar populations with a hierarchical Bayesian approach [53, 54]. The model populations were from the BPASS v2.2 population and spectral synthesis [39] including interacting binaries, adopting a Salpeter initial mass function with a power-law slope of  $\alpha = -2.35$  [108] and a maximum stellar mass of  $300 M_\odot$ . For mono-age populations of  $\log(t/\text{yr}) = 6.0, 6.1, 6.2, \dots$ , BPASS provides number distributions on CMDs [109].

We note that BPASS has only calculated synthetic colors and magnitudes in some selected filter systems (i.e. Johnson-Cousins and HST/WFPC2 filters); those for the HST/ACS and HST/WFC3 filters are not provided. Therefore, we transformed the stellar magnitudes from the observed filters to their closest filters in BPASS (i.e. from WFC3/F555W to WFPC2/F555W). To find the transformation relation, we used PYSYNPHOT to calculate the synthetic magnitudes

of blackbodies with different temperatures and fit the magnitude difference between the two similar filters as a 3rd-order polynomial of color. The magnitude difference is very small (typically  $\lesssim 0.1$  mag for most stars) compared with the photometric uncertainties. Distance, reddening and metallicity were the same as SN 2018gj's. In particular, it is reasonable to assume a uniform extinction across this area since the SN environment is very simple and without recent star formation.

For the  $i$ -th star, its likelihood of belonging to the  $k$ -th population was calculated by comparing its color and magnitude with model predictions on a series of CMDs

$$p^{i,k} = \prod_j p_j^{i,k}, \quad (B1)$$

and

$$p_j^{i,k} = \iint \frac{1}{\sqrt{2\pi}\sigma_{c,j}^i} \exp \left[ -\frac{1}{2} \left( \frac{c_j^i - c_j^{\text{mod}}}{\sigma_{c,j}^i} \right)^2 \right] \times \frac{1}{\sqrt{2\pi}\sigma_{m,j}^i} \exp \left[ -\frac{1}{2} \left( \frac{m_j^i - m_j^{\text{mod}}}{\sigma_{m,j}^i} \right)^2 \right] \times p_j^k(c_j^{\text{mod}}, m_j^{\text{mod}}) dc_j^{\text{mod}} dm_j^{\text{mod}}, \quad (B2)$$

where, in the  $j$ -th CMD,  $m_j^{\text{mod}}$ ,  $m_j^i$  and  $\sigma_{m,j}^i$  are the model magnitude, observed magnitude and its uncertainty;  $c_j^{\text{mod}}$ ,  $c_j^i$  and  $\sigma_{c,j}^i$  are those for the color; and  $p_j^k(c_j^{\text{mod}}, m_j^{\text{mod}})$  is the model probability density distribution. In this work, we used two CMDs of (F555W–F625W, F625W) and (F625W–F814W, F814W), i.e.  $c_1 = m_{\text{F555W}} - m_{\text{F625W}}$ ,  $c_2 = m_{\text{F625W}} - m_{\text{F814W}}$ ,  $m_1 = m_{\text{F625W}}$ , and  $m_2 = m_{\text{F814W}}$ . If a star was not detected in a filter, we could only provide a detection limit for its color and/or magnitude; in this case, we substituted the Gaussian function in (B2) with an error function. For example, if in the  $j$ -th CMD the  $i$ -th star has a magnitude measurement but only a lower limit for its color,  $c_j^i \geq c_j^{\text{lim}} \pm \sigma_{c,j}^{\text{lim}}$ , then  $p_j^{i,k}$  takes the form

$$p_j^{i,k} = \iint \frac{1}{2} \left[ 1 + \text{erf} \left( \frac{c_j^{\text{mod}} - c_j^{\text{lim}}}{\sqrt{2}\sigma_{c,j}^{\text{lim}}} \right) \right] \times \frac{1}{\sqrt{2\pi}\sigma_{m,j}^i} \exp \left[ -\frac{1}{2} \left( \frac{m_j^i - m_j^{\text{mod}}}{\sigma_{m,j}^i} \right)^2 \right] \times p_j^k(c_j^{\text{mod}}, m_j^{\text{mod}}) dc_j^{\text{mod}} dm_j^{\text{mod}}. \quad (B3)$$

The observed stars can be considered as arising from a mixture of mono-age populations, each having a relative weight of  $w_k$ , i.e. the fraction of observed stars belonging to the  $k$ -th population. The weights then provide information of the stellar age distribution in the SN environment. In a hierarchical Bayesian framework, their posterior probability distributions can be expressed as

$$p(w_1, w_2, w_3, \dots | \text{data}) = \prod_i^{N_{\text{star}}} \left( \sum_k^{N_{\text{pop}}} w_k p^{i,k} \right), \quad (B4)$$

where we have adopted a flat prior for the weights of different mono-age populations. We used a Markov-Chain Monte-Carlo (MCMC) method to solve for the posterior probability distributions.

### Appendix C: Hydrodynamical modeling for bolometric light curves

The multi-band photometric data of SN 2018gj were taken from Ref. [33], and the UV–optical–IR (pseudo-)bolometric light curve was reconstructed using the SUPERBOL package [110]. The blackbody-corrected light curve was adopted for our analysis. As shown in Fig. 6, we present the bolometric light curve together with the model predictions from MESA and STELLA, following a similar approach to Ref. [33] but with the initial mass updated to  $15 M_{\odot}$ .

### Appendix D: Initial parameters of the binary system

From our modeled systems, we find that approximately 0.1% of all successful core–collapse SNe in our population would match the observational properties of SN 2018gj within uncertainties based on a Gaussian treatment of the observational constraints on the luminosity, effective temperature, final He-core mass, final H-envelope mass, and age

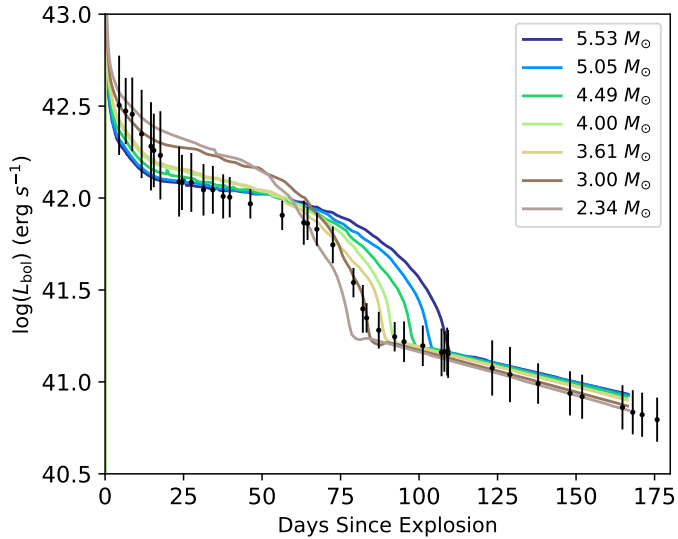


Fig. 6: The UV-optical-IR pseudo-bolometric light curve of SN 2018gj. The observations (black points) are compared with models (color-coded by final H-envelope mass) for which the wind mass-loss rate scaling factor was varied from 2.25 to 3.70 in steps of 0.25.

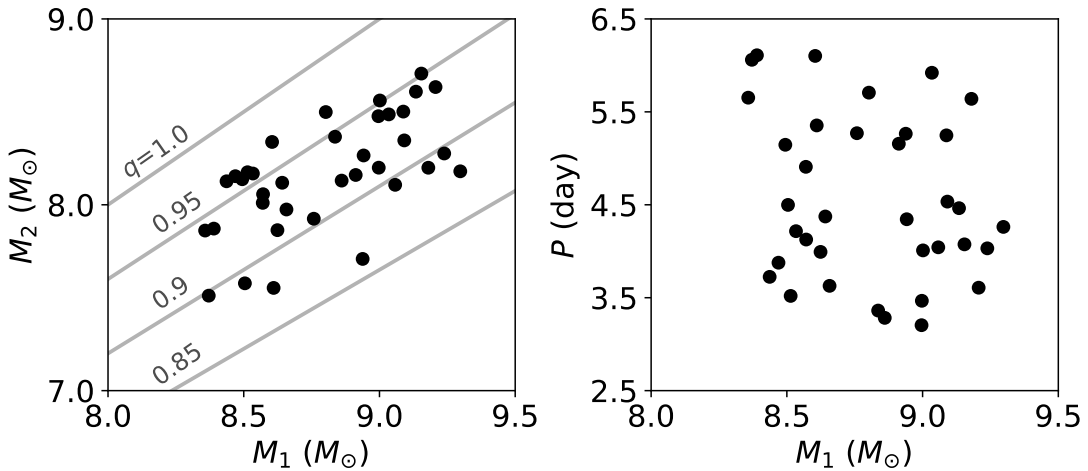


Fig. 7: Initial primary mass ( $M_1$ ), secondary mass ( $M_2$ ) and orbital period for possible reverse-merger models that match the observed constraints for SN 2018gj's progenitor. For reference, the gray lines of constant secondary-to-primary mass ratios ( $q$ ) are plotted in the left panel.

of SN 2018gj's progenitor. Their initial parameters distributions are shown in Fig. 7. This suggests that SN 2018gj-like explosions form a small but non-negligible subset of the broader short-plateau Type II-P population, which itself represents roughly  $\sim 4\text{--}5\%$  of core-collapse SNe in theoretical studies (e.g., [21, 111, 112]) and a few percent observationally (e.g., [113]). A full comparison with the complete short-plateau SN population is outside the scope of this work.

[1] Li W, Leaman J, Chornock R, et al. Nearby supernova rates from the Lick Observatory Supernova Search - II. The observed luminosity functions and fractions of supernovae in a complete sample. *Mon Not R Astron Soc*

2011;412:1441–1472.  
[2] Martinez L, Bersten M C, Anderson J P, et al. Type II supernovae from the Carnegie Supernova Project-I. I. bolometric light curves of 74 SNe II using uBgVriYJH

photometry. *Astron Astrophys* 2022;660:A40.

[3] Martinez L, Bersten M C, Anderson J P, et al. Type II supernovae from the Carnegie Supernova Project-I. II. Physical parameter distributions from hydrodynamical modelling. *Astron Astrophys* 2022;660:A41.

[4] Martinez L, Anderson J P, Bersten M C, et al. Type II supernovae from the Carnegie Supernova Project-I. III. Understanding SN II diversity through correlations between physical and observed properties. *Astron Astrophys* 2022;660:A42.

[5] Smartt S J. Progenitors of core-collapse supernovae. *Annu Rev Astron Astrophys* 2009;47:63–106.

[6] Rui L, Wang X, Mo J, et al. Probing the final-stage progenitor evolution for Type IIP supernova 2017eaw in NGC 6946. *Mon Not R Astron Soc* 2019;485:1990–2000.

[7] Niu Z, Sun N C, Maund J R, et al. The dusty red supergiant progenitor and the local environment of the Type II SN 2023ixf in M101. *Astrophys J Lett* 2023; 955:L15.

[8] Xiang D, Mo J, Wang X, et al. The red supergiant progenitor of Type II supernova 2024ggi. *Astrophys J Lett* 2024;969:L15.

[9] Sana H, de Mink S E, de Koter A, et al. Binary interaction dominates the evolution of massive stars. *Science* 2012;337:444.

[10] Podsiadlowski P, Joss P C, Hsu J J L. Presupernova evolution in massive interacting binaries. *Astrophys J* 1992;391:246.

[11] Maund J R, Smartt S J, Kudritzki R P, et al. The massive binary companion star to the progenitor of supernova 1993J. *Nature* 2004;427:129–131.

[12] Eldridge J J, Fraser M, Smartt S J, et al. The death of massive stars - II. Observational constraints on the progenitors of Type Ibc supernovae. *Mon Not R Astron Soc* 2013;436:774–795.

[13] Yoon S C, Dessart L, Clocchiatti A. Type Ib and IIf supernova progenitors in interacting binary systems. *Astrophys J* 2017;840:10.

[14] Zapartas E, de Mink S E, Van Dyk S D, et al. Predicting the presence of companions for stripped-envelope supernovae: the case of the Broad-lined Type Ic SN 2002ap. *Astrophys J* 2017;842:125.

[15] Sun N C, Maund J R, Hirai R, et al. Origins of Type Ibn SNe 2006jc/2015G in interacting binaries and implications for pre-SN eruptions. *Mon Not R Astron Soc* 2020;491:6000–6019.

[16] Sun N C, Maund J R, Crowther P A. The changing-type SN 2014C may come from an  $11\text{-M}_\odot$  star stripped by binary interaction and violent eruption. *Mon Not R Astron Soc* 2020;497:5118–5135.

[17] Sun N C, Maund J R, Crowther P A, et al. An environmental analysis of the Type Ib SN 2019yvr and the possible presence of an inflated binary companion. *Mon Not R Astron Soc* 2022;510:3701–3715.

[18] Sun N C, Maund J R, Crowther P A. A UV census of the environments of stripped-envelope supernovae. *Mon Not R Astron Soc* 2023;521:2860–2873.

[19] Niu Z, Sun N C, Liu J. Discovery of a dusty yellow supergiant progenitor for the Type IIf SN 2017gkk. *Astrophys J Lett* 2024;970:L9.

[20] Zhao Y H, Sun N C, Wu J, et al. Exclusion of a direct progenitor detection for the Type Ic SN 2017ein based on late-time observations. *Astrophys J Lett* 2025; 980:L6.

[21] Eldridge J J, Xiao L, Stanway E R, et al. Supernova lightCURVE POPulation synthesis I: including interacting binaries is key to understanding the diversity of type II supernova lightcurves. *Publ Astron Soc Aust* 2018; 35:e049.

[22] Zapartas E, de Mink S E, Justham S, et al. The diverse lives of progenitors of hydrogen-rich core-collapse supernovae: the role of binary interaction. *Astron Astrophys* 2019;631:A5.

[23] Dessart L, Gutiérrez C P, Ercolino A, et al. A sequence of Type Ib, IIf, II-L, and II-P supernovae from binary-star progenitors with varying initial separations. *Astron Astrophys* 2024;685:A169.

[24] Schneider F R N, Podsiadlowski P, Laplace E. Presupernova evolution and final fate of stellar mergers and accretors of binary mass transfer. *Astron Astrophys* 2024;686:A45.

[25] Ercolino A, Jin H, Langer N, et al. The demographics of core-collapse supernovae I. The role of binary evolution and CSM interaction. *arXiv*: 2510.04872, 2025.

[26] Farrell E J, Groh J H, Meynet G, et al. The uncertain masses of progenitors of core-collapse supernovae and direct-collapse black holes. *Mon Not R Astron Soc* 2020; 494:L53–L58.

[27] Zapartas E, Fox O D, Su J, et al. The demographics of binary companions to stripped-envelope supernovae: confronting population synthesis models with observations. *Mon Not R Astron Soc* 2025;.

[28] Schneider F R N, Podsiadlowski P, Langer N, et al. Rejuvenation of stellar mergers and the origin of magnetic fields in massive stars. *Mon Not R Astron Soc* 2016; 457:2355–2365.

[29] Zapartas E, de Mink S E, Izzard R G, et al. Delay-time distribution of core-collapse supernovae with late events resulting from binary interaction. *Astron Astrophys* 2017;601:A29.

[30] Zapartas E, de Mink S E, Justham S, et al. Effect of binary evolution on the inferred initial and final core masses of hydrogen-rich, Type II supernova progenitors. *Astron Astrophys* 2021;645:A6.

[31] Bostroem K A, Zapartas E, Koplitz B, et al. Considering the single and binary origins of the Type IIP SN 2017eaw. *Astron J* 2023;166:255.

[32] Schneider F R N, Ohlmann S T, Podsiadlowski P, et al. Long-term evolution of a magnetic massive merger product. *Mon Not R Astron Soc* 2020;495:2796–2812.

[33] Teja R S, Singh A, Sahu D K, et al. SN 2018gj: a short plateau type II supernova with persistent blueshifted H $\alpha$  emission. *Astrophys J* 2023;954:155.

[34] van Dokkum P G. Cosmic-ray rejection by Laplacian edge detection. *Publ Astron Soc Pac* 2001;113:1420–1427.

[35] McCully C, Crawford S, Kovacs G, et al. astropy/astroscrappy: v1.0.5 zenodo release, 2018.

[36] Dolphin A E. WFPC2 stellar photometry with HST-PHOT. *Publ Astron Soc Pac* 2000;112:1383–1396.

[37] Van Dyk S D, Lee J C, Anderson J, et al. LEGUS discovery of a light echo around supernova 2012aw. *Astrophys J* 2015;806:195.

[38] Gustafsson B, Edvardsson B, Eriksson K, et al. A grid of MARCS model atmospheres for late-type stars. I. Methods and general properties. *Astron Astrophys* 2008; 486:951–970.

[39] Eldridge J J, Stanway E R, Xiao L, et al. Binary Population and Spectral Synthesis Version 2.1: construction, observational verification, and new results. *Publ Astron Soc Aust* 2017;34:e058.

[40] Izzard R G, Tout C A, Karakas A I, et al. A new synthetic model for asymptotic giant branch stars. *Mon Not R Astron Soc* 2004;350:407–426.

[41] Fragos T, Andrews J J, Bavera S S, et al. POSYDON: a general-purpose population synthesis code with detailed binary-evolution simulations. *Astrophys J Suppl* 2023; 264:45.

[42] Andrews J J, Bavera S S, Briel M, et al. POSYDON Version 2: Population Synthesis with Detailed Binary-evolution Simulations across a Cosmological Range of Metallicities. *Astrophys J Suppl* 2025;281:3.

[43] Fang Q, Moriya T J, Maeda K. Red supergiant problem viewed from the nebular phase spectroscopy of type II supernovae. *Astrophys J* 2025;986:39.

[44] Morozova V, Piro A L, Valenti S. Measuring the progenitor masses and dense circumstellar material of Type II supernovae. *Astrophys J* 2018;858:15.

[45] Goldberg J A, Bildsten L, Paxton B. A massive star’s dying breaths: pulsating red supergiants and their resulting Type IIP supernovae. *Astrophys J* 2020;891:15.

[46] Bronner V A, Laplace E, Schneider F R N, et al. Explosions of pulsating red supergiants: A natural pathway for the diversity of Type II-P/L supernovae. *Astron Astrophys* 2025;703:A61.

[47] Van Dyk S D, Zheng W, Maund J R, et al. The Type II-plateau supernova 2017eaw in NGC 6946 and its red supergiant progenitor. *Astrophys J* 2019;875:136.

[48] Zimmerman E A, Irani I, Chen P, et al. The complex circumstellar environment of supernova 2023ixf. *Nature* 2024;627:759–762.

[49] Laplace E, Bronner V A, Schneider F R N, et al. Pulsations change the structures of massive stars before they explode: interpreting the nearby supernova SN 2023ixf. *arXiv*: 2508.11088, 2025.

[50] Kilpatrick C D, Suresh A, Davis K W, et al. The Type II SN 2025pht in NGC 1637: A Red Supergiant with Carbon-rich Circumstellar Dust as the First JWST Detection of a Supernova Progenitor Star. *Astrophys J Lett* 2025;992:L10.

[51] Valenti S, Howell D A, Stritzinger M D, et al. The diversity of Type II supernova versus the similarity in their progenitors. *Mon Not R Astron Soc* 2016;459:3939–3962.

[52] Hicken M, Friedman A S, Blondin S, et al. Type II supernova light curves and spectra from the CfA. *Astrophys J Suppl* 2017;233:6.

[53] Maund J R, Ramirez-Ruiz E. A high mass progenitor for the Type Ic supernova 2007gr inferred from its environment. *Mon Not R Astron Soc* 2016;456:3175–3185.

[54] Sun N C, Maund J R, Crowther P A, et al. Towards a better understanding of supernova environments: a study of SNe 2004dg and 2012P in NGC 5806 with HST and MUSE. *Mon Not R Astron Soc* 2021;504:2253–2272.

[55] Renzo M, Zapartas E, de Mink S E, et al. Massive runaway and walkaway stars. A study of the kinematical imprints of the physical processes governing the evolution and explosion of their binary progenitors. *Astron Astrophys* 2019;624:A66.

[56] Wagg T, Dalcanton J J, Renzo M, et al. Delayed and Displaced: The Impact of Binary Interactions on Core-collapse SN Feedback. *Astron J* 2025;170:192.

[57] Boubert D, Guillochon J, Hawkins K, et al. Revisiting hypervelocity stars after Gaia DR2. *Mon Not R Astron Soc* 2018;479:2789–2795.

[58] Marchetti T, Evans F A, Rossi E M. Gaia DR3 in 6D: the search for fast hypervelocity stars and constraints on the galactic centre environment. *Mon Not R Astron Soc* 2022;515:767–774.

[59] Paxton B, Bildsten L, Dotter A, et al. Modules for experiments in stellar astrophysics (MESA). *Astrophys J Suppl* 2011;192:3.

[60] Blinnikov S, Sorokina E. Type Ia supernova models: latest developments. *Astrophys Space Sci* 2004;290:13–28.

[61] Dessart L, Hillier D J. The difficulty of inferring progenitor masses from type-II-Plateau supernova light curves. *Astron Astrophys* 2019;625:A9.

[62] Davies B, Plez B, Petrucci M. Explosion imminent: the appearance of red supergiants at the point of core-collapse. *Mon Not R Astron Soc* 2022;517:1483–1490.

[63] Morozova V, Piro A L, Valenti S. Measuring the progenitor masses and dense circumstellar material of Type II supernovae. *Astrophys J* 2018;858:15.

[64] Fang Q, Maeda K, Ye H, et al. Diversity in hydrogen-rich envelope mass of Type II supernovae. I. Plateau phase light-curve modeling. *Astrophys J* 2025;978:35.

[65] Goldberg J A, Bildsten L. The value of progenitor radius measurements for explosion modeling of Type II-Plateau supernovae. *Astrophys J Lett* 2020;895:L45.

[66] Utrobin V P, Chugai N N. Revisiting short-plateau SN 2018gj. *Astrophys Space Sci* 2024;369:49.

[67] Sukhbold T, Woosley S E. The compactness of presupernova stellar cores. *Astrophys J* 2014;783:10.

[68] Heger A, Fryer C L, Woosley S E, et al. How massive single stars end their life. *Astrophys J* 2003;591:288–300.

[69] Crowther P A. Physical properties of Wolf-Rayet stars. *Annu Rev Astron Astrophys* 2007;45:177–219.

[70] Izzard R G, Tout C A, Karakas A I, et al. A new synthetic model for asymptotic giant branch stars. *Mon Not R Astron Soc* 2004;350:407–426.

[71] Izzard R G, Dray L M, Karakas A I, et al. Population nucleosynthesis in single and binary stars. I. model. *Astron Astrophys* 2006;460:565–572.

[72] Izzard R G, Glebbeek E, Standcliffe R J, et al. Population synthesis of binary carbon-enhanced metal-poor stars. *Astron Astrophys* 2009;508:1359–1374.

[73] Beasor E R, Davies B, Smith N, et al. A new mass-loss rate prescription for red supergiants. *Mon Not R Astron Soc* 2020;492:5994–6006.

[74] Zapartas E, de Wit S, Antoniadis K, et al. The effect of mass loss in models of red supergiants in the Small Magellanic Cloud. *Astron Astrophys* 2025;697:A167.

[75] Ekström S, Georgy C, Eggenberger P, et al. Grids of stellar models with rotation. I. Models from 0.8 to 120  $M_{\odot}$  at solar metallicity ( $Z = 0.014$ ). *Astron Astrophys* 2012;537:A146.

[76] Kaiser E A, Hirschi R, Arnett W D, et al. Relative importance of convective uncertainties in massive stars. *Mon Not R Astron Soc* 2020;496:1967–1989.

[77] Brott I, de Mink S E, Cantiello M, et al. Rotating massive main-sequence stars. I. Grids of evolutionary models and isochrones. *Astron Astrophys* 2011;530:A115.

[78] Hurley J R, Pols O R, Tout C A. Comprehensive ana-

lytic formulae for stellar evolution as a function of mass and metallicity. *Mon Not R Astron Soc* 2000;315:543–569.

[79] Paxton B, Cantiello M, Arras P, et al. Modules for Experiments in Stellar Astrophysics (MESA): planets, oscillations, rotation, and massive stars. *Astrophys J Suppl* 2013;208:4.

[80] Paxton B, Marchant P, Schwab J, et al. Modules for Experiments in Stellar Astrophysics (MESA): binaries, pulsations, and explosions. *Astrophys J Suppl* 2015; 220:15.

[81] Paxton B, Schwab J, Bauer E B, et al. Modules for Experiments in Stellar Astrophysics (MESA): convective boundaries, element diffusion, and massive star explosions. *Astrophys J Suppl* 2018;234:34.

[82] Paxton B, Smolec R, Schwab J, et al. Modules for Experiments in Stellar Astrophysics (MESA): pulsating variable stars, rotation, convective boundaries, and energy conservation. *Astrophys J Suppl* 2019;243:10.

[83] Webbink R F. Double white dwarfs as progenitors of R Coronae Borealis stars and type I supernovae. *Astrophys J* 1984;277:355–360.

[84] Livio M, Soker N. The common envelope phase in the evolution of binary stars. *Astrophys J* 1988;329:764.

[85] Patton R A, Sukhbold T. Towards a realistic explosion landscape for binary population synthesis. *Mon Not R Astron Soc* 2020;499:2803–2816.

[86] Ertl T, Janka H T, Woosley S E, et al. A two-parameter criterion for classifying the explodability of massive stars by the neutrino-driven mechanism. *Astrophys J* 2016;818:124.

[87] Ivanova N, Justham S, Ricker P. Common Envelope Evolution. IOP Publishing, Bristol, UK, 2020.

[88] Auchettl K, Lopez L A, Badenes C, et al. Measurement of the Core-collapse progenitor mass distribution of the Small Magellanic Cloud. *Astrophys J* 2019;871:64.

[89] Murphy J W, Barrientos A F, Andrae R, et al. The mass of the Vela Pulsar progenitor and the age of the Vela-Puppis complex. *Astrophys J* 2025;988:241.

[90] Castrillo A, Ascasibar Y, Galbany L, et al. The delay time distribution of supernovae from integral-field spectroscopy of nearby galaxies. *Mon Not R Astron Soc* 2021;501:3122–3136.

[91] Schootemeijer A, Götberg Y, de Mink S E, et al. Clues about the scarcity of stripped-envelope stars from the evolutionary state of the sdO+Be binary system  $\varphi$  Persei. *Astron Astrophys* 2018;615:A30.

[92] Fryer C L, Heger A. Binary merger progenitors for Gamma-Ray bursts and Hypernovae. *Astrophys J* 2005; 623:302–313.

[93] Tout C A, Wickramasinghe D T, Lau H H B, et al. A common envelope binary star origin of long gamma-ray bursts. *Mon Not R Astron Soc* 2011;410:2458–2462.

[94] Stanway E R, Eldridge J J. Re-evaluating old stellar populations. *Mon Not R Astron Soc* 2018;479:75–93.

[95] Falco E E, Kurtz M J, Geller M J, et al. The Updated Zwicky Catalog (UZC). *Publ Astron Soc Pac* 1999;111:438–452.

[96] Mould J R, Huchra J P, Freedman W L, et al. The Hubble Space Telescope Key Project on the Extragalactic Distance Scale. XXVIII. Combining the constraints on the Hubble constant. *Astrophys J* 2000;529:786–794.

[97] Riess A G, Yuan W, Macri L M, et al. A comprehensive measurement of the local value of the Hubble constant with  $1 \text{ km s}^{-1} \text{ Mpc}^{-1}$  uncertainty from the Hubble Space Telescope and the SH0ES Team. *Astrophys J Lett* 2022;934:L7.

[98] Schlafly E F, Finkbeiner D P. Measuring reddening with Sloan Digital Sky Survey stellar spectra and recalibrating SFD. *Astrophys J* 2011;737:103.

[99] Cardelli J A, Clayton G C, Mathis J S. The relationship between infrared, optical, and ultraviolet extinction. *Astrophys J* 1989;345:245.

[100] van Driel W, Buta R J. A study of the ringed galaxies NGC 2273, 4826 and 6217. *Astron Astrophys* 1991; 245:7.

[101] Storchi-Bergmann T, Calzetti D, Kinney A L. Ultraviolet to near-infrared spectral distributions of star-forming galaxies: metallicity and age effects. *Astrophys J* 1994; 429:572.

[102] Lu S, Zhu K, Cappellari M, et al. MaNGA DynPop - II. Global stellar population, gradients, and star-formation histories from integral-field spectroscopy of 10K galaxies: link with galaxy rotation, shape, and total-density gradients. *Mon Not R Astron Soc* 2023;526:1022–1045.

[103] Patterson M T, Walterbos R A M, Kennicutt R C, et al. An oxygen abundance gradient into the outer disc of M81. *Mon Not R Astron Soc* 2012;422:401–419.

[104] Vink J S, de Koter A, Lamers H J G L M. Mass-loss predictions for O and B stars as a function of metallicity. *Astronomy and Astrophysics* 2001;369:574–588. ISSN 0004-6361.

[105] Antoniadis K, Bonanos A Z, de Wit S, et al. Establishing a mass-loss rate relation for red supergiants in the Large Magellanic Cloud. *Astron Astrophys* 2024; 686:A88.

[106] Götberg Y, de Mink S E, Groh J H. Ionizing spectra of stars that lose their envelope through interaction with a binary companion: role of metallicity. *Astron Astrophys* 2017;608:A11.

[107] Hovis-Afflerbach B, Götberg Y, Schootemeijer A, et al. The mass distribution of stars stripped in binaries: the effect of metallicity. *arXiv e-prints* 2024; arXiv:2412.05356.

[108] Salpeter E E. The luminosity function and stellar evolution. *Astrophys J* 1955;121:161.

[109] Stevance H. Bpassv2.2.1 starter kit, 2022.

[110] Nicholl M. SuperBol: a user-friendly Python routine for bolometric light curves. *Research Notes of the American Astronomical Society* 2018;2:230.

[111] Eldridge J J, Guo N Y, Rodrigues N, et al. Supernova lightCURVE POPulation synthesis II: validation against supernovae with an observed progenitor. *Publ Astron Soc Aust* 2019;36:e041.

[112] Hiramatsu D, Howell D A, Moriya T J, et al. Luminous Type II short-plateau supernovae 2006Y, 2006ai, and 2016egz: a transitional class from stripped massive red supergiants. *Astrophys J* 2021;913:55.

[113] Anderson J P, González-Gaitán S, Hamuy M, et al. Characterizing the V-band light-curves of hydrogen-rich Type II supernovae. *Astrophys J* 2014;786:67.